

Enhanced Light Trapping and Power Conversion Efficiency in Ultrathin Plasmonic Organic Solar Cells: A Coupled Optical-Electrical Multiphysics Study on the Effect of Nanoparticle Geometry

Sungjun In,[†] Daniel R. Mason,[†] Hyunho Lee,[‡] Mi Jung,[§] Changhee Lee,[‡] and Namkyoo Park^{*,†}

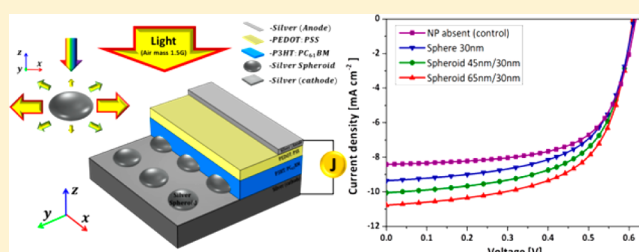
[†]Photonic Systems Laboratory and [‡]Organic Semiconductor Laboratory, School of EECS, Seoul National University, Seoul 151-744, South Korea

[§]Sensor System Research Center, Korea Institute of Science and Technology, Seoul 136-791, South Korea

S Supporting Information

ABSTRACT: Plasmonic effects associated with localized surface plasmon (LSP) resonances such as strong light trapping, large scattering cross-section, and giant electric field enhancement have received much attention for the more efficient harvesting of solar energy. Notably, even as the thickness of the active layer is significantly reduced, the optical absorption capability of a solar cell could be maintained with the incorporation of plasmonic effects. This is especially important for the development of bulk heterojunction (BHJ) organic solar cells (OSCs), where the short exciton diffusion length, low carrier mobility, and strong charge recombination in organic materials strongly favors the use of optically thin active layers (<100 nm). However, the disappointing performance improvements obtained with plasmonic effects in the majority of BHJ OSCs realized to date suggests that plasmonic effects are yet to be fully taken advantage of; for example, in thick active layer OSCs (>100 nm), the optical absorption is already high, even in the absence of plasmonic effects, while in thin active layer OSCs (<100 nm), insufficient attention has been given to the analysis of plasmonic effects, such as the impact of plasmonic nanoparticle (NP) geometrical factors on the directional scattering efficiency. In this paper, we propose and demonstrate that the geometrical tuning of *spheroidal* plasmonic nanoparticles (NPs) could enable the full exploitation of plasmonic effects, providing dramatic improvements to the light absorption and energy harvesting capability of ultrathin film BHJ OSCs. Our theoretical analysis demonstrates a dramatic enhancement in optical absorption of ~60% with spheroidal NPs embedded in a BHJ OSC device with ultrathin, <100 nm active layer, as compared to an NP absent reference device. These improvements are explained according to enhanced scattering of light into the active layer plane, spectral broadening of absorption resonances, in addition to an increased plasmonic modal volume, exhibited near LSP resonances of spheroidal NPs with optimal eccentricity. The result of our coupled optical-electrical device simulations also proves that the outstanding optical absorption enhancement obtained from the proposed device indeed translates into significant electrical performance gains; such as a ~30% increase in the short-circuit current and ~20% improvement in the power conversion efficiency (PCE).

KEYWORDS: photovoltaics, localized surface plasmon, organic solar cells, plasmonics, metallic nanoparticles, device physics



Bulk heterojunction organic solar cells with active layers comprising regioregular mixtures of polymer donor and fullerene acceptor materials have been envisioned as a promising next generation energy harvesting device due to their lightweight, mechanical robustness, and low-cost, all-solution processing and fabrication.^{1–6} Nonetheless, currently inhibiting the wide scale emergence of BHJ OSCs is the poor carrier mobility and short exciton diffusion length in organic semiconductors that restricts their active layer to very small thicknesses, greatly diminishing their optical absorption and power conversion efficiency (PCE) to well below that of their inorganic counterparts (e.g., those based on Si, GaAs, CdTe, Cu(In, Ga)Se₂, etc.). Efforts to address this issue have been thrust in two main directions. One of these emphasizes improvement of the constituent materials and their morpho-

logical implementation, such as development of new donor/acceptor organic materials^{7–11} or the introduction of efficient hole/electron transport layers via new process/postfabrication treatments,^{11–13} and numerous morphological optimizations^{2–5,14,15} (e.g., advanced heterojunction structure and blend network). The other main direction has been toward improving the optical absorption capability of the device, especially in the active layer, through the introduction of plasmonic effects utilizing the strong field localization and scattering of metallic nanostructures. For example, localized surface plasmon (LSP) resonances supported by metallic gratings,^{16,17,33} nanostructures,^{18,19} and nanoparticles

Received: July 22, 2014

Published: December 2, 2014

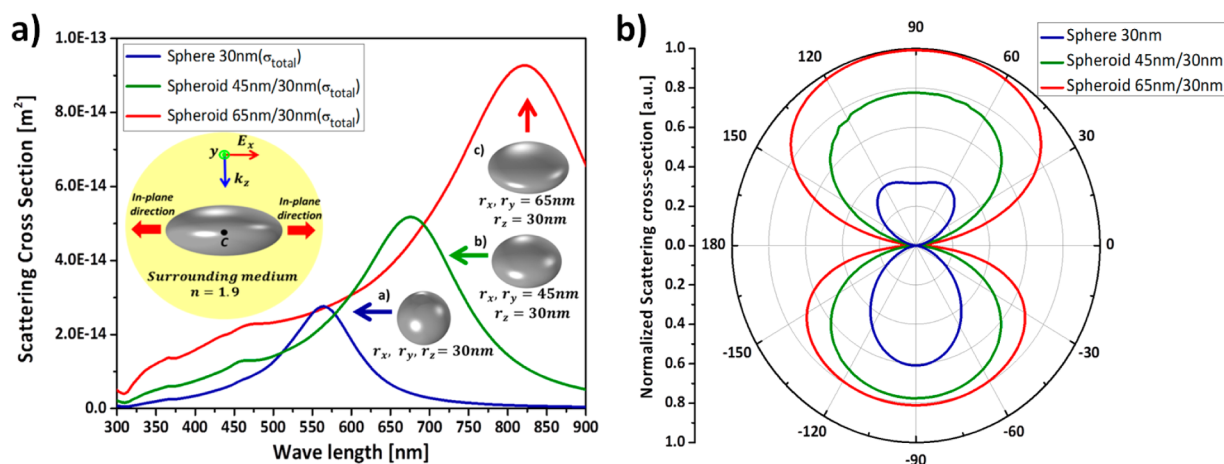


Figure 1. (a) Wavelength dependence of total scattering cross section (σ_{scatt}) of an isolated spheroidal NP immersed in a uniform medium with refractive index $n = 1.9$, at several different eccentricities: Sphere ($e = 0$), slight oblate spheroid ($e = 0.75$), and optimized spheroid ($e = 0.89$). Left inset shows schematic diagram of simulation geometry and incident plane wave propagation direction and polarization. (b) Polar plot of scattering intensity summed (at each angle) over wavelengths $300 \text{ nm} \leq \lambda \leq 900 \text{ nm}$ and normalized to the maximum value of the optimized spheroid.

(NPs)^{20–22,30–32,34–36} embedded in the active layer, and their electromagnetic coupling to a metallic backplane electrode to form hybridized plasmonic resonances,^{23–26} have been shown to enhance light absorption in the active layer. Of special note are theoretical and experimental studies of OSCs loaded with various compositions, shapes, and geometrical arrangements of plasmonic nanoparticles such as cooperative Ag–Au NPs,²⁷ dual-plasmonic nano structures,¹⁶ various shape NPs,^{20,21,28} and shell-coated silver NPs,²² which could be manufactured and deposited entirely using simple and low-cost all-solution processes.^{11,29} Nevertheless, most of these studies have focused on the incorporation of NPs into optically thick active layers ($>100 \text{ nm}$) resulting in minor performance gains with plasmonic effects. Indeed, for the challenging design of OSCs with ultrathin active layers ($<100 \text{ nm}$), insufficient attention and efforts were made so far for the full exploitation of plasmonic effects, for example, to the geometrical factors of NPs that provide optimal light trapping conditions, specifically tailored for ultrathin solar cell applications. Moreover, only very few theoretical studies have presented coupled optical-electrical multiphysics modeling for both plasmonic inorganic and organic solar cells, which to-date has included grating,^{49,51} Ag back corrugation⁶⁵ and metal NP loaded devices,⁵⁰ yet it is the only route toward the precise modeling and assessment of the role of plasmonic effects in the actual device performance.

Here we propose and theoretically demonstrate that the introduction of *spheroidal* nanoparticles with optimal eccentricity into ultrathin ($<100 \text{ nm}$) BHJ OSCs can dramatically enhance their light harvesting capability by improving the optical absorption in the active layer by up to $\sim 60\%$. Our rigorous optical-electrical coupled numerical calculations show that the eccentricity of spheroids plays a crucial role by increasing the directionality of scattered light into the plane of the active layer, as compared to their purely spherical counterparts. From our newly developed coupled optical-electrical multiphysics model implemented in COMSOL, we show that the improved optical absorption capability of OSCs with spheroidal NPs translates into a PCE enhancement of $\sim 20\%$ compared to an NP absent reference device. This work demonstrates that ultrathin OSCs with plasmonic NPs can provide comparable optical absorption capability to those based on much (several times) thicker active layers, and constitutes,

to our knowledge, the largest predicted plasmonic enhancement of optical absorption in organic solar cells.

RESULTS AND DISCUSSION

We start by discussing the effects of spheroid eccentricity on the directionality of scattering and LSP resonances of metallic spheroidal NPs. Figure 1a shows finite element method (FEM) calculations (see Methods) of the total scattering cross section (σ_{scatt}) for an isolated Ag spheroid immersed in a bulk medium of refractive index $n = 1.9$ (the average index of common BHJ OSC active layer material P3HT:PC₆₁BM in the considered wavelength range $300 \text{ nm} \leq \lambda \leq 800 \text{ nm}$) when illuminated by a plane wave propagating in the direction of the spheroid minor axis (see inset of Figure 1a), at several different eccentricities. The eccentricity parameter (e) is defined $ase^2 = 1 - r_z^2/r_{xy}^2$, where r_z is the minor axis and r_{xy} are the lengths of the major axes. The curves in Figure 1a correspond respectively to a sphere ($e = 0$, $r = 30 \text{ nm}$), slight oblate spheroid ($e = 0.75$, $r_x = r_y = 45 \text{ nm}$, $r_z = 30 \text{ nm}$), and the optimized spheroid ($e = 0.89$, $r_x = r_y = 65 \text{ nm}$, $r_z = 30 \text{ nm}$); the optimized spheroid is that which is shown below to provide the maximum plasmonic enhancement of PCE in the considered OSCs. The maximum of σ_{scatt} at each eccentricity seen in Figure 1a corresponds to the dipolar LSP resonance of the spheroidal NP (see Supporting Information, Figure S1). Increasing the eccentricity is seen to provide an overall increase of σ_{scatt} across the entire spectral range, and a broadened, red-shifted LSP resonance. Figure 1b shows the scattering pattern of each spheroid, obtained by summing the pointing vector flux at a given angle θ (the polar angle describing the x – z plane) over the considered wavelength range and normalizing to the maximum value of the optimized spheroid. Interestingly, an increased eccentricity of the spheroid results in more light being scattered into the plane parallel to the spheroid major axis (i.e., the xy plane), which we denote as the in-plane direction. Indeed, the percentage of energy scattered into the angular ranges $-45 \leq \theta \leq 45$ and $135 \leq \theta \leq 225$ (degrees) is 22.5, 30.3, and 36.8%, for $e = 0$, 0.75, and 0.89, respectively. The origin of the improved in-plane scattering is well explained by the increase of uniaxial polarizabilities (α_{xy}), as evident from the expression $\alpha_k = 4\pi a^2(\epsilon_{\text{NP}}(\omega) - \epsilon_s)/(3\epsilon_s + 3L_k(\epsilon_{\text{NP}}(\omega) - \epsilon_s))$, $\kappa = x, y, z$, where $\epsilon_{\text{NP}}(\omega)$ and ϵ_s are the permittivities of the spheroid NP and

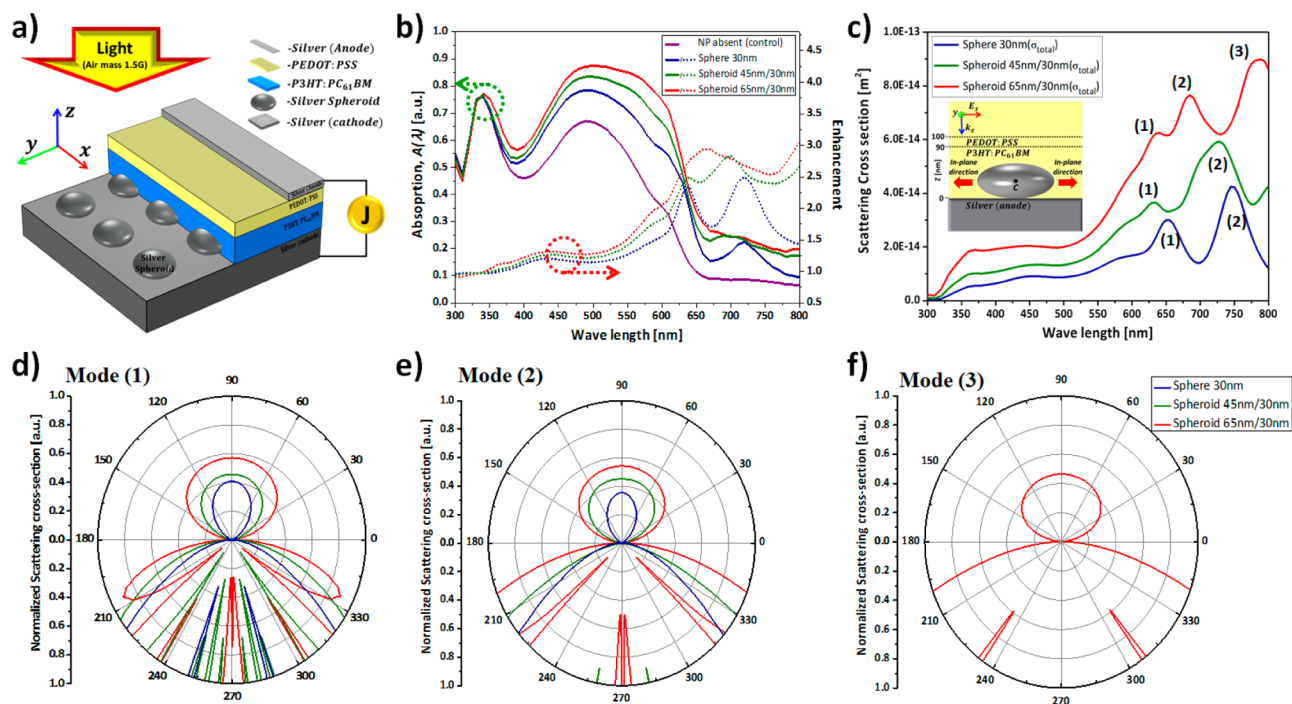


Figure 2. (a) Schematic diagram of proposed bulk heterojunction plasmonic organic solar cell: silver (anode, positioned near device edges)/PEDOT:PSS/P3HT:PC₆₁BM with or without silver NPs array/silver (cathode). (b) Wavelength dependence of percentage optical absorption (solid curves) and absorption enhancement (dotted curves) for spheroidal NPs as in Figure 1: NP absent reference BHJ OSCs (purple curves), sphere NPs (blue curves; $P = 200$ nm, $r = 30$ nm), slight oblate spheroid NPs (green curves; $P = 210$ nm, $r_x = r_y = 45$ nm, $r_z = 30$ nm), and optimized spheroid NPs (red curves; $P = 230$ nm, $r_x = r_y = 65$ nm, $r_z = 30$ nm). (c) Wavelength dependence of total scattering cross section (σ_{scat}) of NPs in BHJ OSCs optimized at each spheroid eccentricity. Left inset shows schematic diagram of simulation geometry. (d–f) Polar plot of scattering intensity normalized to the maximum value of the optimized spheroid: (d) mode (1), (e) mode (2), and (f) mode (3).

surrounding medium, and L_k is the geometrical factors given by $L_k = g(e)/2e^2[\pi/2 - \tan^{-1} g(e)] - g^2(e)/2$, $g(e) = ((1 - e^2)/e^2)^{1/2}$ with $L_x + L_y + L_z = 1$, and $L_x = L_y$ in an oblate spheroid.^{37,38,40} From these expressions we find that an increase of the eccentricity leads to both an enhancement of the in-plane polarizability ($\alpha_{x,y}$) compared to that along the minor axis (α_z), and a red shift of the $\alpha_{x,y}$ polarizability resonance. We note that the relative increase in $\alpha_{x,y}$ over α_z physically manifests as an increased surface charge concentration that builds up around opposing points of the spheroid equator, becoming more evident as the eccentricity is increased (see Figure S1); compare with the sphere where the induced charges are more evenly spread out with azimuthal symmetry. This broken azimuthal symmetry of charge accumulation in the oblate spheroid leads to a departure of the scattering pattern from the classical dipolar scattering pattern exhibited by a sphere, skewing it toward the in-plane direction. We also note that the increased surface charge density in the spheroid case can as well provide regions with significantly larger plasmonic enhancement of electric field compared to the regions of electric field enhancement nearby the sphere (see below).

Considering the above results, we hypothesize that loading oblate spheroidal NPs into a thin active layer of a BHJ OSC (with the spheroid major axis parallel to the active layer) would increase its optical absorption capability by directing more of the incident light into the in-plane direction of the active layer. The proposed BHJ OSC device is presented in Figure 2a: a 90 nm thick P3HT:PC₆₁BM active layer coated with a 10 nm thick PEDOT:PSS hole transport layer, sits atop a bulk Ag substrate (cathode). The thin Ag wire network (anode) serves as an electrical contact at the device edges and is not considered

in the optical simulations. In the optimization, we adjust the thickness of the active layer, as well as the period between NPs to achieve maximum plasmonic enhancement of the PCE. The optimization process is as follows: For a given periodic spheroid NP array, using the finite element method (FEM) calculations,⁴⁴ we calculate the absorption spectrum from which we determine the short circuit current weighted according to the AM1.5G incident solar irradiance. Then, in an equivalent thickness of the controlled BHJ OSC, we optimize a period of the loaded spheroid for the greatest PCE from the device. It is important to note that there do exist device parameter sets that provide larger optical absorption (e.g., 55.27%, and PCE 3.84%, at 65–30 nm oblate spheroid with period 210 nm) than our stated optimal structure, although the overall optical-electrical optimal design point of the device was found at 65–30 nm oblate spheroid with period 230 nm (PCE 4.02%, optical absorption of 53.6%). All presented results correspond to the optimal (with respect to PCE) thickness of active layer (90 nm) and period of spheroid placement: $P = 200, 210, 230$, for $e = 0, 0.75$, and 0.89 , respectively. It is also noted that since each oblate spheroid is rotationally symmetric about its minor axis which is parallel to z , and since the spheroids are arranged into a square lattice as shown in Figure 2a, the absorption and scattering spectrum of the array is invariant on rotation of the structure by 90° in the x – y plane (with respect to a fixed incident wave). Figure 2b shows the percentage absorption (i.e., the ratio of number of photons absorbed to number of incident photons at a given wavelength) in the active layer, excluding metallic absorption, and the absorption enhancement of the NP loaded OSCs as compared to an NP absent reference structure (with all other geometric parameters the same), when the

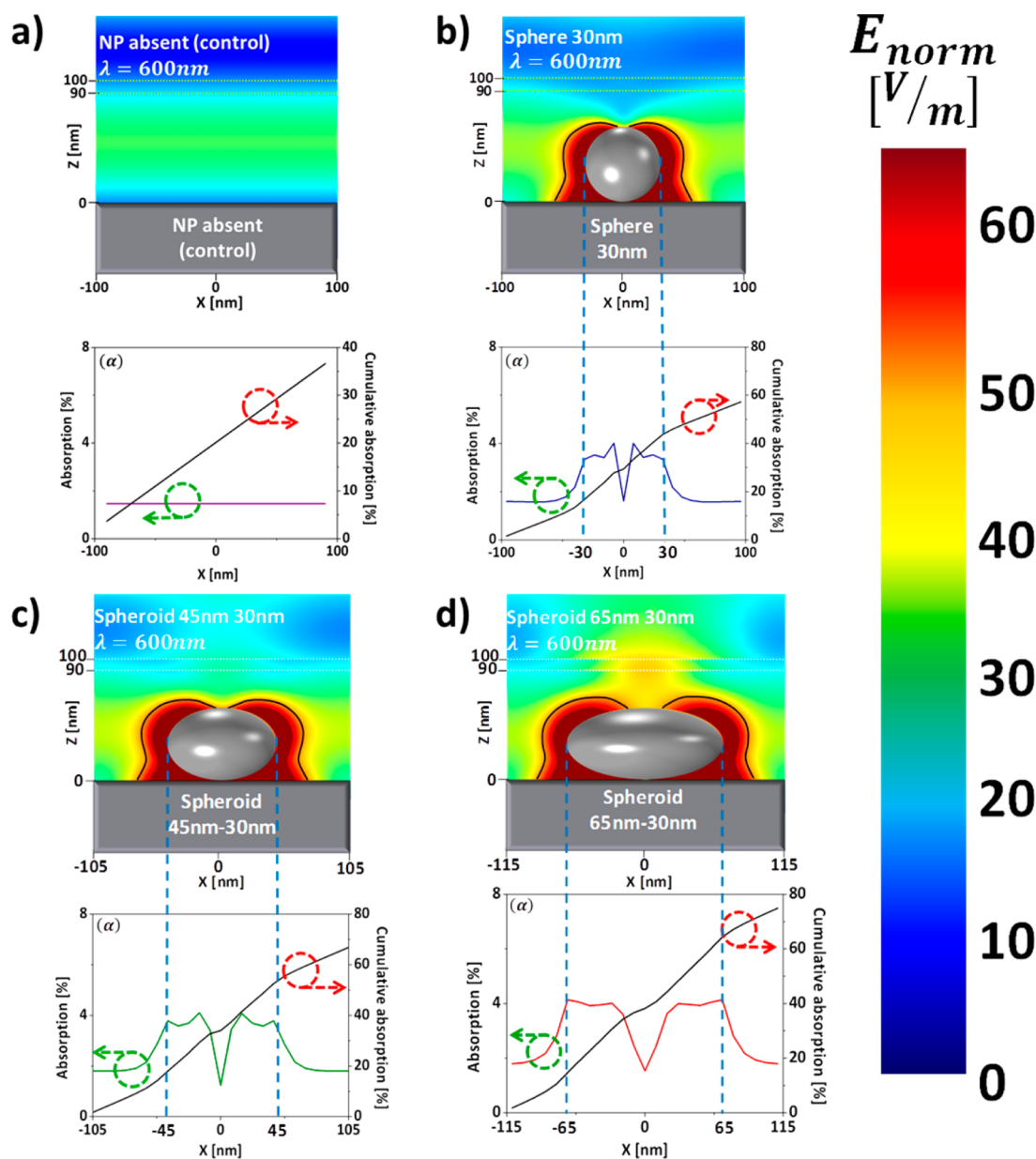


Figure 3. Calculated electric field distributions ($|E|$, left-upper side of each panel) of (a) NP absent reference case, (b) sphere case, (c) slight oblate spheroid case, and (d) optimized spheroid case at $\lambda = 600$ nm. (Insets) x -Dependent absorption and cumulative absorption as defined in the main text. Black contour curve demarcates region where the volume of the near-field region contains strong electric fields, as defined in text.

OSCs are illuminated by normally incident light with power weighted according to the AM1.5G solar spectrum. Here we can see that the inclusion of spheroidal NPs with eccentricity increasing toward the optimal value (red curve) provides dramatically increased absorption as compared to both the NP absent reference (purple curve) and the spherical NP case (blue curve): the cumulative improvements to absorption are found to be 57.6% and 18.8%, respectively, from integrating the absorption over the considered spectral range. Furthermore, we note that these improvements to the optical absorption are sustained at large oblique angles of $-70 \leq \theta \leq 70$ (degrees) (see Supporting Information), guaranteeing effective all-day usage of the device.

It is evident from Figure 2b that the spheroidal NPs impact the absorption spectrum in two main ways. First, they greatly improve light trapping in the active layer within the main absorption peak of P3HT:PC₆₁BM where $400 \text{ nm} \leq \lambda \leq 630$

nm. Second, at longer wavelengths $\lambda > 630$ nm, the apparent resonant peaks in the absorption enhancement are significantly broadened by increased spheroid eccentricity. To assess the physical origins of absorption enhancement in the considered device, we start by confirming whether the enhanced in-plane scattering is preserved when NPs are placed in the vicinity of a metallic substrate. In Figure 2c we show the scattering cross section of an individual Ag spheroidal NP embedded in the device (i.e., as an element of the array) at several eccentricities. In comparison with Figure 1a, σ_{scat} for each spheroid in the device now exhibits a broad background resonance corresponding to the spheroid LSP mode, onto which is superposed several narrow maxima corresponding to successive orders of hybridization between the spheroid LSP mode and its image charges in the metallic substrate (see Figure S3), which we denote as hybridized gap modes (HGMs).^{41,42,68,70} The increased eccentricity of the spheroid, providing a smaller

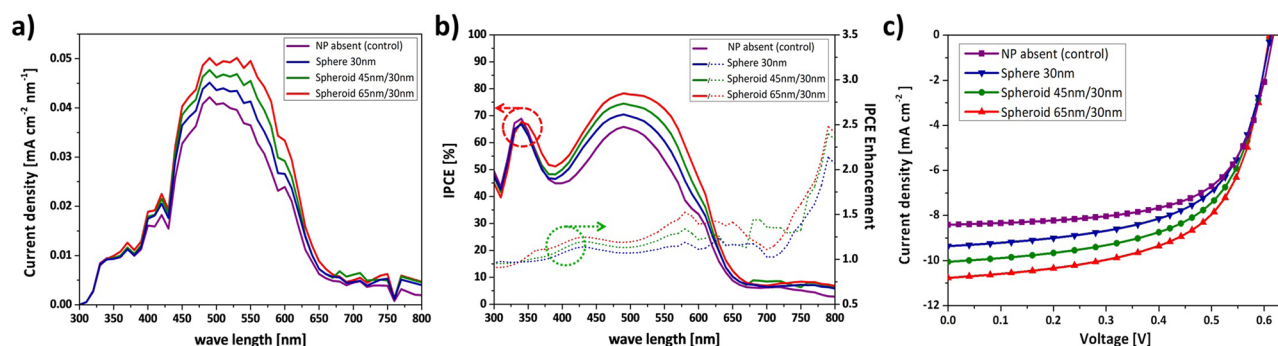


Figure 4. (a) Wavelength dependence of J_{sc} for NP absent reference (purple curves), sphere NPs (blue curves), slight oblate spheroid NPs (green curves), and optimized spheroid NPs (red curves); (b) Wavelength dependence of IPCE (solid curves) and IPCE enhancement (dotted curves); (c) J – V characteristics of BHJ OSCs for devices in (a) and (b). All data corresponds to AM 1.5G weighted normally incident plane wave illumination.

average distance between the substrate and NP surface, leads to a blue shift and broadening of the HGM resonances, in good agreement with previous reports on HGMs.⁴³ The scattering patterns of modes (1), (2), and (3) at their respective resonant wavelengths, presented in Figure 2d–f, show that the HGMs also exhibit enhanced in-plane scattering when the spheroid eccentricity is increased. Indeed, the scattering into the cumulative angular range $-45 \leq \theta \leq 45$, $135 \leq \theta \leq 225$ (degrees) by the optimal spheroid was calculated to be ~ 1.8 (HGM mode (1)) and ~ 3.7 (HGM mode (2)) times that of the spheres ($e = 0$), in which light is most prominently directed toward or away from the Ag substrate. Thus, we may conclude, on comparing Figure 2c with Figure 2b, that improved in-plane scattering of the spheroids with increased eccentricity near the HGM resonances is primarily responsible for the dramatic enhancements to the absorption of the device at longer wavelengths $\lambda > 630$ nm. Furthermore, we note that the overall increase of the scattering cross-section to the left of the LSP resonance exhibited at increased eccentricity also provides significant enhancements to the optical absorption at shorter wavelengths $\lambda \leq 630$ nm. At higher eccentricity than the optimal value, while an even broader enhancement of scattering could be possible, the increased ohmic losses due to the increased metal volume in the active layer eventually start to reduce the PCE of the solar cell.

Besides increased in-plane scattering, local electric field enhancement in the near-field region of spheroids at the HGM resonances will also contribute to improved absorption in the active layer, since the local electron–hole-pair production rate is proportional to the local electric field intensity. In Figure 3 we show color maps of the electric field magnitude inside the (a) NP absent reference and (b–d) spheroidal NP loaded devices with $e = 0, 0.75$, and 0.89 , under normally incident illumination; the wavelength of the incident light was chosen to be $\lambda = 600$ nm which is near the absorption peak labeled (1) in Figure 2c. Insets of each panel in Figure 3 show the x -dependent optical absorption (i.e., $A_X(\lambda, x) = \int_{AL} A_{loc}(\lambda, x, y, z) dy dz$, where $A_{loc}(\lambda, x, y, z)$ is the local optical absorption in a unit cell, and AL denotes integration across the active layer for y , and film thickness for z) and cumulative absorption $\int_{-P/2}^x A_X(\lambda, x') dx'$; P is the period of the structure, and integration is across the active layer for x). It is apparent by comparing Figures 3b–d that an increase in the spheroid eccentricity (and, an associated increase in r_x and r_y) has significantly increased the volume of the near-field region that contains strong electric field; this is explicitly shown by the contour demarcating regions where $|E| \geq 2 \times |E_{max}| \exp(-1)$.

Indeed, calculations of the active layer volumes enclosed by the contours in Figure 3b–d shows that the modal volume of the optimal spheroid is ~ 1.8 times larger than that of spheres ($e = 0$) when normalized to the total active layer volume.

Having demonstrated the superior light collection capability of our proposed spheroidal NP loaded BHJ OSC, we now determine the actual device performance by calculating its electrical characteristics (see Methods). Our electrical model takes as input the exciton generation rate, G_{opt} , which can be calculated directly from the local electric field intensity (see Figure S6), and enters as a source term in coupled Poisson and continuity equations. The coupled Poisson–continuity system of equations is solved using FEM to obtain the short circuit current (J_{sc}), incident photon to electron conversion efficiency (IPCE), and current density–voltage (J – V) characteristics. Figure 4a,b shows the spectral response of J_{sc} , IPCE, and IPCE enhancement for both spheroidal NP loaded and NP absent reference devices. Similar in form to the absorption spectra, we find that the IPCE exceeds 70% in the range $440 \text{ nm} < \lambda < 630 \text{ nm}$, while J_{sc} is significantly enhanced in the broadband range $340 \text{ nm} < \lambda < 800 \text{ nm}$; the sharp drop off of J_{sc} outside this region is understood according to the weak incident solar irradiation power at short wavelengths. The plot of IPCE enhancement factor in Figure 4b is closely coincident with the spectra of the absorption enhancement factor in Figure 2b, demonstrating that the plasmonic enhancement provided by the Ag spheroids is responsible for the performance increase. The J – V characteristics of NP loaded devices and the reference device is also shown in Figure 4c.

Summarized in Table 1 are quantitative details of the device electrical performance. The reference device exhibits a power conversion efficiency of 3.36%, an open-circuit voltage of 0.618 V, a short circuit current 8.41 mA/cm², and a fill factor (FF; $J_{max} V_{max} / J_{sc} V_{oc}$) of 64.7%, in reasonable agreement with previous experimental reports.^{4,9–11} Meanwhile, our proposed BHJ OSC with optimized spheroidal NPs shows a power

Table 1. Electrical Performance Characteristics of OSCs Extracted from Coupled Optical–Electrical Device Simulations

case	J_{sc} (mA/cm ²)	V_{oc} (V)	FF (%)	PCE (%)
NP absent (control)	8.41	0.618	64.7	3.36
sphere	9.36	0.612	61.4	3.52
slight oblate spheroid	10.05	0.611	61.2	3.76
optimized spheroid	10.77	0.611	61.1	4.02

conversion efficiency of 4.02%, an open-circuit voltage of 0.611 V, a short circuit current of 10.77 mA/cm², and a FF of 61.1%. In comparison with the reference device, this constitutes very large improvements to J_{sc} and PCE; approaching ~30 and ~20%, respectively. It is noted that the device with optimized spheroids also significantly outperforms the spherical ($\epsilon = 0$) NP loaded device, exhibiting ~15% and ~14% improvements in J_{sc} and PCE, respectively, thus, proving the importance of the geometrical optimization of NPs in deriving the best device performance of ultrathin solar cells, in this case, through the modal volume increase and in-plane scattering maximization. While BHJ OSCs with P3HT:PC₆₁BM active layers having PCEs of 4–5% have been reported,^{4,5,11,15,21} it is emphasized that the PCE of 4% in our proposed device is a significant achievement, considering that the active layer is ultrathin by a factor of ~1.5–3^{1,11,15,21} (assuming the same materials).

CONCLUSIONS

In conclusion, we have proposed, systematically analyzed, and demonstrated a simple and novel approach for maximizing plasmonic enhancement in organic solar cells, challenging the obstacles of weak optical absorption and short electrical carrier diffusion lengths. Under the setting of spheroidal metallic nanoparticles embedded in ultrathin active layers of conventional P3HT:PC₆₁BM OSCs, we have suggested and demonstrated enhancement of scattering into the ultrathin active layer plane, and increased near-field volumes of strong optical absorption; which together dramatically improve the optical absorption of organic solar cells. Dramatic improvements of ~60% to the optical absorption, ~30% to the short-circuit current, and ~20% to the PCE in the proposed device as compared to a nanoparticle absent reference, have been demonstrated using coupled optical-electrical FEM numerical analysis of the device. The proposed platform of spheroidal metallic nanoparticles should be applicable to various ultrathin semiconducting materials opening opportunities for a range of highly efficient bulk heterojunction organic solar cells.

MATERIALS AND METHODS

Coupled Optical–Electrical Device Simulations. All simulations were performed using the finite element method (FEM) implemented in COMSOL Multiphysics.⁴⁴ Simulations consisted of two parts sharing a common FEM mesh. First, an optical part which solves Maxwell's equations for specified illumination conditions and whose output is the electric field intensity $|E(x,y,z)|^2$. And second, an electrical part which solves the coupled Poisson and charge carrier continuity equations with $|E(x,y,z)|^2$ taken as input. Optical parameters included complex refractive indices of P3HT:PC₆₁BM and PEDOT:PSS taken from refs 26 and 45, and dielectric permittivity of Ag modeled using a Lorentz–Drude fit to the measured data from Palik,⁴⁶ and the incident illumination intensity was spectrally weighted according to the AM1.5G solar spectrum. Electrical parameters included exciton lifetime (τ_x) taken from ref 47, diffusion coefficient (D_x) taken from ref 48 and 67, reaction cross sections (σ_{x-n} , σ_{x-p}) and reaction velocity (v_x) taken from refs 51 and 52, electron and hole mobility (μ_n , μ_p) taken from refs 53 and 54, lifetime (τ_n , τ_p) taken from ref 55, band gap taken from refs 56 and 57, work function taken from refs 51 and 58.

In the optical simulations, perfectly matched layers (PML) were used at the top and bottom unit cell boundaries, and

periodic boundary conditions between neighboring unit cells. In electrical simulations, the P3HT:PC₆₁BM/Ag and P3HT:PC₆₁BM/PEDOT:PSS interfaces were included as ohmic and Schottky contact boundary conditions, respectively, and periodic boundary conditions between neighboring unit cells. The exciton generation rate (in the active layer) is given by $G_{opt}(\lambda) = ((\epsilon''|E(\lambda,x,y,z)|)/(2\hbar))$, where ϵ'' is the imaginary part of dielectric permittivity, and \hbar is the reduced Planck constant. Due to the disordered polymeric nature of P3HT:PC₆₁BM, charge transport is modeled as a stochastic hopping process with Gaussian energy distribution.^{54,57,59,60} The spatially dependent electron or hole mobility is a function of local electric field magnitude according to the Poole-Frenkel model:^{61,66} $\mu(E,T) = \mu_0 \exp(\gamma((E^{1/2})/(T)))$, where μ_0 is the zero-field mobility, γ is a material related activation energy, and T is the temperature. The coupled Poisson, and exciton, electron, and hole continuity equations are given by

$$\nabla^2 \phi = \frac{q(p - n + N_d^+ - N_a^-)}{\epsilon} \quad (1)$$

$$\frac{\partial x}{\partial t} = G + R - D - \frac{x - x_{eq}}{\tau_x} + \frac{1}{q} \nabla(D_x \nabla x) \quad (2)$$

$$\frac{\partial n}{\partial t} = D - R - \frac{n - n_{eq}}{\tau_n} - \frac{1}{q} \nabla(qn\mu_n \nabla \phi - k_B T \mu_n \nabla n) \quad (3)$$

$$\frac{\partial p}{\partial t} = D - R - \frac{p - p_{eq}}{\tau_p} + \frac{1}{q} \nabla(qn\mu_p \nabla \phi + k_B T \mu_p \nabla p) \quad (4)$$

where k_B is the Boltzmann constant, ϕ is the electrostatic potential, D_x is the exciton diffusion coefficient, μ_n and μ_p are the electron and hole mobilities, N_d^+ and N_a^- are the concentration of ionized donors and acceptors, and p , n , and x are the densities, p_{eq} , n_{eq} , and x_{eq} are the equilibrium densities, and τ_n , τ_p , and τ_x are the lifetimes of electrons, holes, and excitons, respectively. We note that the band-to-band Langevin bimolecular recombination,⁶² trap-assisted Shockley–Read–Hall (SRH) recombination⁶³ and surface recombination⁵⁶ are included in the continuity equations (eqs 2–4); deep trap states are not considered, which is a common assumption in the modeling of plasmonic solar cells. These states negligibly contribute to the space charges field.^{49,51,52,54} For the dissociation rate, we use the Staudigel's dissociation⁶⁴ expressions, which include local changes in the exciton density due to interactions with holes and electrons. More specific simulation details of the electrical simulation part such as determination of preillumination electronic equilibrium parameters can be found in refs 51, 52, and 56. J – V curves are obtained by applying a potential difference between top and bottom boundaries of the unit cell. From these J – V curves, we can calculate all standard solar cell performance parameters, such as J_{sc} , V_{oc} , FF, IPCE, and PCE.

Scattering Cross-Section Calculations. For the single isolated particle in a homogeneous medium, we use PMLs at the computational boundaries under the scattered field formulation. For particles in the BHJ solar cell structure, simulation conditions were as described in the previous Methods, and a two-step scattered field formulation was used.^{43,69}

The scattering cross section is then calculated by its definition:³⁹

$$\sigma_{\text{total,sc}} = \frac{1}{I_0} \iint (\mathbf{n} \cdot \mathbf{S}_{\text{total,sc}}) dS \quad (5)$$

where \mathbf{n} is the vector normal pointing outward from the surface of integration, $\mathbf{S}_{\text{total,sc}}$ is the Poynting vector calculated from the scattered field, I_0 is the incident intensity, and the integral is evaluated over the particle surface.

■ ASSOCIATED CONTENT

■ Supporting Information

This material contains surface charge distributions of spheroidal dipolar resonance, scattering spectra for NPs of different radii, surface charge distributions of BHJ OSCs loaded with NPs, definition of FOM, electric field distribution at $\lambda = 730$ nm, absorption dependence on illumination angle, and exciton generation maps. This material is available free of charge via the Internet at <http://pubs.acs.org>.

■ AUTHOR INFORMATION

Corresponding Author

*E-mail: nkpark@snu.ac.kr.

Notes

The authors declare no competing financial interest.

■ ACKNOWLEDGMENTS

This work was supported by the Brain Korea 21 Plus Project in 2014 and the National Research Foundation of Korea (NRF) under the Ministry of Science, ICT & Future Planning, the Global Frontier Program NRF-2014M3A6B3063708, the Global Research Laboratory (GRL) Program K20815000003 (2008-00580), and the Global Frontier R&D Program by the Center for Multiscale Energy Systems 2011-0031561, all funded by the South Korean government.

■ REFERENCES

- (1) Li, G.; Shrotriya, V.; Huang, J.; Yao, Y.; Moriarty, T.; Emery, K.; Yang, Y. High-Efficiency Solution Processable Polymer Photovoltaic Cells by Self-Organization of Polymer Blends. *Nat. Mater.* **2005**, *4*, 864–868.
- (2) Park, S. H.; Roy, A.; Beaupré, S.; Cho, S.; Coates, N.; Moon, J. S.; Heeger, A. J. Bulk Heterojunction Solar Cells with Internal Quantum Efficiency Approaching 100%. *Nat. Photonics* **2009**, *3*, 297–302.
- (3) Ye, L.; Zhang, S.; Ma, W.; Fan, B.; Guo, X.; Huang, Y.; Hou, J. From Binary to Ternary Solvent: Morphology Fine-Tuning of D/A Blends in PDPP3T-Based Polymer Solar Cells. *Adv. Mater.* **2012**, *24*, 6335–6341.
- (4) Liu, B.; Png, R. Q.; Zhao, L. H.; Chua, L. L.; Friend, R. H.; Ho, P. K. High Internal Quantum Efficiency in Fullerene Solar Cells Based on Crosslinked Polymer Donor Networks. *Nat. Commun.* **2012**, *3*, 1321.
- (5) Zhang, X.; Lu, Z.; Ye, L.; Zhan, C.; Hou, J.; Zhang, S.; Yao, J. A Potential Perylene Diimide Dimer-Based Acceptor Material for Highly Efficient Solution-Processed Non-Fullerene Organic Solar Cells with 4.03% Efficiency. *Adv. Mater.* **2013**, *25*, 5791–5797.
- (6) Thompson, B. C.; Fréchet, J. M. Polymer–Fullerene Composite Solar Cells. *Angew. Chem., Int. Ed.* **2008**, *47*, 58–77.
- (7) Andrew, T. L.; Bulovic, V. Bulk Heterojunction Solar Cells Containing 6,6-Dicyanofulvenes as n-Type Additives. *ACS Nano* **2012**, *6*, 4671–4677.
- (8) Chu, T. Y.; Lu, J.; Beaupré, S.; Zhang, Y.; Pouliot, J. R.; Wakim, S.; Tao, Y. Bulk Heterojunction Solar Cells Using Thieno[3,4-c]pyrrole-4,6-dione and Dithieno[3,2-b:2',3'-d']silole Copolymer with a Power Conversion Efficiency of 7.3%. *J. Am. Chem. Soc.* **2011**, *133*, 4250–4253.
- (9) Lobez, J. M.; Andrew, T. L.; Bulovic, V.; Swager, T. M. Improving the Performance of P3HT–Fullerene Solar Cells with Side-Chain-

Functionalized Poly (Thiophene) Additives: a New Paradigm for Polymer Design. *ACS Nano* **2012**, *6*, 3044–3056.

(10) Khlyabich, P. P.; Burkhart, B.; Thompson, B. C. Compositional Dependence of the Open-Circuit Voltage in Ternary Blend Bulk Heterojunction Solar Cells Based on Two Donor polymers. *J. Am. Chem. Soc.* **2012**, *134*, 9074–9077.

(11) Ameri, T.; Khoram, P.; Min, J.; Brabec, C. J. Organic Ternary Solar cells: a Review. *Adv. Mater.* **2013**, *25*, 4245–4266.

(12) Kyaw, A. K. K.; Wang, D. H.; Wynands, D.; Zhang, J.; Nguyen, T. Q.; Bazan, G. C.; Heeger, A. J. Improved Light Harvesting and Improved Efficiency by Insertion of an Optical Spacer (ZnO) in Solution-Processed Small-Molecule Solar Cells. *Nano Lett.* **2013**, *13*, 3796–3801.

(13) Xu, X.; Cai, P.; Lu, Y.; Choon, N. S.; Chen, J.; Hu, X.; Ong, B. S. Synthesis and Characterization of Thieno[3,2-b]thiophene-Isoindigo-Based Copolymers as Electron Donor and Hole Transport Materials for Bulk-Heterojunction Polymer Solar Cells. *J. Polym. Sci., Part A: Polym. Chem.* **2013**, *51*, 424–434.

(14) Wong, H. C.; Li, Z.; Tan, C. H.; Zhong, H.; Huang, Z.; Bronstein, H.; Durrant, J. R. Morphological Stability and Performance of Polymer–Fullerene Solar Cells Under Thermal Stress—The Impact of Photoinduced PC60BM Oligomerisation. *ACS Nano* **2014**, *8*, 1297–1308.

(15) Park, H. J.; Lee, J. Y.; Lee, T.; Guo, L. J. Advanced Heterojunction Structure of Polymer Photovoltaic Cell Generating High Photocurrent with Internal Quantum Efficiency Approaching 100%. *Adv. Energy Mater.* **2013**, *3*, 1135–1142.

(16) Li, X.; Choy, W. C.; Huo, L.; Xie, F.; Sha, W. E.; Ding, B.; Yang, Y. Dual Plasmonic Nanostructures for High Performance Inverted Organic Solar Cells. *Adv. Mater.* **2012**, *24*, 3046–3052.

(17) You, J.; Li, X.; Xie, F. X.; Sha, W. E.; Kwong, J. H.; Li, G.; Yang, Y. Surface Plasmon and Scattering-Enhanced Low-Bandgap Polymer Solar Cell by a Metal Grating Back Electrode. *Adv. Energy Mater.* **2012**, *2*, 1203–1207.

(18) Lee, S.; In, S.; Mason, D. R.; Park, N. Incorporation of Nanovoids into Metallic Gratings for Broadband Plasmonic Organic Solar Cells. *Opt. Express* **2013**, *21*, 4055–4060.

(19) Niesen, B.; Rand, B. P.; Van Dorpe, P.; Cheyng, D.; Tong, L.; Dmitriev, A.; Heremans, P. Plasmonic Efficiency Enhancement of High Performance Organic Solar Cells with a Nanostructured Rear Electrode. *Adv. Energy Mater.* **2013**, *3*, 145–150.

(20) Wang, D. H.; Park, K. H.; Seo, J. H.; Seifter, J.; Jeon, J. H.; Kim, J. K.; Park, J. H.; Park, O. O.; Heeger, A. J. Enhanced Power Conversion Efficiency in PCDTBT/PC70BM Bulk Heterojunction Photovoltaic Devices with Embedded Silver Nanoparticle Clusters. *Adv. Energy Mater.* **2011**, *1*, 766–770.

(21) Li, X.; Choy, W. C. H.; Lu, H.; Sha, W. E. I.; Ho, A. H. P. Efficiency Enhancement of Organic Solar Cells by Using Shape-Dependent Broadband Plasmonic Absorption in Metallic Nanoparticles. *Adv. Funct. Mater.* **2013**, *23*, 2728–2735.

(22) Choi, H.; Lee, J. P.; Ko, S. J.; Jung, J. W.; Park, H.; Yoo, S.; Kim, J. Y. Multipositional Silica-Coated Silver Nanoparticles for High-Performance Polymer Solar Cells. *Nano Lett.* **2013**, *13*, 2204–2208.

(23) Lee, S.; Mason, D. R.; In, S.; Park, N. Embedding Metal Electrodes in Thick Active Layers for ITO-Free Plasmonic Organic Solar Cells with Improved Performance. *Opt. Express* **2014**, *22*, A1145–A1152.

(24) Chou, S. Y.; Ding, W. Ultrathin, High-Efficiency, Broad-Band, Omni-Acceptance, Organic Solar Cells Enhanced by Plasmonic Cavity with Subwavelength Hole Array. *Opt. Express* **2013**, *21*, A60–A76.

(25) Kang, M. G.; Xu, T.; Park, H. J.; Luo, X.; Guo, L. J. Efficiency Enhancement of Organic Solar Cells Using Transparent Plasmonic Ag Nanowire Electrodes. *Adv. Mater.* **2010**, *22*, 4378–4383.

(26) Shen, H.; Maes, B. Combined Plasmonic Gratings in Organic Solar Cells. *Opt. Express* **2011**, *19*, A1202–A1210.

(27) Lu, L.; Luo, Z.; Xu, T.; Yu, L. Cooperative Plasmonic Effect of Ag and Au Nanoparticles on Enhancing Performance of Polymer Solar Cells. *Nano Lett.* **2012**, *13*, 59–64.

- (28) Kulkarni, A. P.; Noone, K. M.; Munechika, K.; Guyer, S. R.; Ginger, D. S. Plasmon-Enhanced Charge Carrier Generation in Organic Photovoltaic Films Using Silver Nanoprisms. *Nano Lett.* **2010**, *10*, 1501–1505.
- (29) Gan, Q.; Bartoli, F. J.; Kafafi, Z. H. Plasmonic-Enhanced Organic Photovoltaics: Breaking the 10% Efficiency Barrier. *Adv. Mater.* **2013**, *25*, 2385–2396.
- (30) Akimov, Y. A.; Koh, W. S.; Ostrikov, K. Enhancement of Optical Absorption in Thin-Film Solar Cells through the Excitation of Higher-order Nanoparticle Plasmon Modes. *Opt. Express* **2009**, *17* (12), 10195–10205.
- (31) Lee, J. Y.; Peumans, P. The Origin of Enhanced Optical Absorption in Solar Cells with Metal Nanoparticles Embedded in the Active Layer. *Opt. Express* **2010**, *18* (10), 10078–10087.
- (32) Wei, E. I.; Choy, W. C.; Liu, Y. G.; Chew, W. C. Near-field Multiple Scattering Effects of Plasmonic Nanospheres Embedded into Thin-Film Organic Solar Cells. *Appl. Phys. Lett.* **2011**, *99* (11), 113304.
- (33) Sha, W. E.; Choy, W. C.; Chew, W. C. A Comprehensive Study for the Plasmonic Thin-Film Solar Cell with Periodic Structure. *Opt. Express* **2010**, *18* (6), 5993–6007.
- (34) Zhu, J.; Xue, M.; Hoekstra, R.; Xiu, F.; Zeng, B.; Wang, K. L. Light Concentration and Redistribution in Polymer Solar Cells by Plasmonic Nanoparticles. *Nanoscale* **2012**, *4* (6), 1978–1981.
- (35) Wei, E. I.; Choy, W. C.; Liu, Y. G.; Chew, W. C. Near-Field Multiple Scattering Effects of Plasmonic Nanospheres Embedded into Thin-film Organic Solar Cells. *Appl. Phys. Lett.* **2011**, *99* (11), 113304.
- (36) Baek, S. W.; Noh, J.; Lee, C. H.; Kim, B.; Seo, M. K.; Lee, J. Y. Plasmonic Forward Scattering Effect in Organic Solar Cells: A Powerful Optical Engineering Method. *Sci. Rep.* **2013**, *3*, 1726.
- (37) Mie, G. Beiträge zur Optik Trüber Medien, Speziell Kolloidaler Metallösungen. *Ann. Phys.* **1908**, *25*, 377–445.
- (38) Asano, S.; Yamamoto, G. Light Scattering by a Spheroidal Particle. *Appl. Opt.* **1975**, *14*, 29–49.
- (39) Bohren, C. F.; Huffman, D. R. *Absorption and Scattering of Light by Small Particles*; John Wiley & Sons: New York, 1983.
- (40) Flammer, C. *Spheroidal Wave Functions*; Stanford University Press: New York, 1957.
- (41) Lei, D. Y.; Fernandez-Dominguez, A. I.; Sonnefraud, Y.; Appavoo, K.; Haglund, R. F.; Pendry, J. B.; Maier, S. A. Revealing Plasmonic Gap Modes in Particle-on-Film Systems Using Dark-Field Spectroscopy. *ACS Nano* **2012**, *6*, 3537–3544.
- (42) Yamamoto, N.; Ohtani, S.; García de Abajo, F. J. Gap and Mie Plasmons in Individual Silver Nanospheres Near a Silver Surface. *Nano Lett.* **2010**, *11*, 91–95.
- (43) Noguez, C. Surface Plasmons on Metal Nanoparticles: the Influence of Shape and Physical Environment. *J. Phys. Chem. C* **2007**, *111*, 3806–3819.
- (44) Comsol Multiphysics, <http://www.comsol.com>.
- (45) Shen, H.; Bienstman, P.; Maes, B. Plasmonic Absorption Enhancement in Organic Solar Cells with Thin Active Layers. *J. Appl. Phys.* **2009**, *106*, 073109.
- (46) Palik, E. D. *Handbook of Optical Constants of Solids*; Academic Press: New York, 1985.
- (47) Scheblykin, I. G.; Yartsev, A.; Pullerits, T.; Gulbinas, V.; Sundström, V. Excited State and Charge Photogeneration Dynamics in Conjugated Polymers. *J. Phys. Chem. B* **2007**, *111*, 6303–6321.
- (48) Pirijs, J.; Dykstra, T. E.; Bakulin, A. A.; Loosdrecht, P. H. V.; Knulst, W.; Trinh, M. T.; Siebbeles, L. D. Photogeneration and Ultrafast Dynamics of Excitons and Charges in P3HT/PCBM Blends. *J. Phys. Chem. C* **2009**, *113*, 14500–14506.
- (49) Sha, W. E.; Choy, W. C.; Wu, Y.; Chew, W. C. Optical and Electrical Study of Organic Solar Cells with a 2D Grating Anode. *Opt. Express* **2012**, *20* (3), 2572–2580.
- (50) Li, X.; Hylton, N. P.; Giannini, V.; Lee, K. H.; Ekins-Daukes, N. J.; Maier, S. A. Bridging Electromagnetic and Carrier Transport Calculations for Three-dimensional Modelling of Plasmonic Solar Cells. *Opt. Express* **2011**, *19* (104), A888–A896.
- (51) Vervisch, W.; Rivière, G.; Vedraïne, S.; Biondo, S.; Torchio, P.; Duché, D.; Simon, J.-J.; Escoubas, L. Optical-Electrical Simulation of Organic Solar Cells: Influence of Light Trapping by Photonic Crystal and ZnO Spacer on Electrical Characteristics. *J. Appl. Phys.* **2012**, *111*, 094506.
- (52) Vervisch, W.; Biondo, S.; Rivière, G.; Duché, D.; Escoubas, L.; Torchio, P.; Simon, J.-J.; Rouzo, J. L. Optical-Electrical Simulation of Organic Solar Cells: Excitonic Modeling Parameter Influence on Electrical Characteristics. *Appl. Phys. Lett.* **2011**, *98*, 253306.
- (53) Shuttle, C. G.; O'Regan, B.; Ballantyne, A. M.; Nelson, J.; Bradley, D. D. C.; De Mello, J.; Durrant, J. R. Experimental Determination of the Rate Law for Charge Carrier decay in a Polythiophene: Fullerene Solar Cell. *Appl. Phys. Lett.* **2008**, *92*, 3311.
- (54) Nam, Y. M.; Huh, J.; Jo, W. H. A Computational Study on Optimal Design for Organic Tandem Solar Cells. *Sol. Energy Mater. Sol. Cells* **2011**, *95*, 1095–1101.
- (55) Garcia-Belmonte, G.; Boix, P. P.; Bisquert, J.; Sessolo, M.; Bolink, H. J. Simultaneous Determination of Carrier Lifetime and Electron Density-of-States in P3HT: PCBM Organic Solar Cells under Illumination by Impedance Spectroscopy. *Sol. Energy Mater. Sol. Cells* **2010**, *94*, 366–375.
- (56) Fonash, S. *Solar cell Device Physics*. Elsevier, 2012.
- (57) Kim, J. Y.; Lee, K.; Coates, N. E.; Moses, D.; Nguyen, T. Q.; Dante, M.; Heeger, A. J. Efficient Tandem Polymer Solar Cells Fabricated by All-Solution Processing. *Science* **2007**, *317*, 222–225.
- (58) Dou, L.; You, J.; Yang, J.; Chen, C. C.; He, Y.; Murase, S.; Yang, Y. Tandem Polymer Solar Cells Featuring a Spectrally Matched Low-Bandgap Polymer. *Nat. Photonics* **2012**, *6*, 180–185.
- (59) Bässler, H. Charge Transport in Disordered Organic Photoconductors a Monte Carlo Simulation Study. *Phys. Status Solidi B* **1993**, *175*, 15–56.
- (60) Boland, P.; Lee, K.; Dean, J.; Namkoong, G. Design of Organic Tandem Solar Cells Using Low- and High-Bandgap Polymer: Fullerene Composites. *Sol. Energy Mater. Sol. Cells* **2010**, *94*, 2170–2175.
- (61) Frenkel, J. On Pre-Breakdown Phenomena in Insulators and Electronic Semi-Conductors. *Phys. Rev.* **1938**, *54*, 647.
- (62) Langevin, P. Recombinaison et Mobilités des Ions dans les Gaz. *Ann. Chim. Phys.* **1903**, *28*, 433–530.
- (63) Shockley, W.; Read, W. T. Statistics of the Recombination of Holes and Electrons. *Phys. Rev.* **1952**, *87*, 835.
- (64) Staudigel, J.; Stössel, M.; Steuber, F.; Simmerer, J. A Quantitative Numerical Model of Multilayer Vapor-Deposited Organic Light Emitting Diodes. *J. Appl. Phys.* **1999**, *86*, 3895–3910.
- (65) Deceglie, M. G.; Ferry, V. E.; Alivisatos, A. P.; Atwater, H. A. Design of Nanostructured Solar Cells Using Coupled Optical and Electrical Modeling. *Nano Lett.* **2012**, *12* (6), 2894–2900.
- (66) Melzer, C.; Koop, E. J.; Mihailetschi, V. D.; Blom, P. W. Hole Transport in Poly (Phenylene Vinylene)/Methanofullerene Bulk-Heterojunction Solar Cells. *Adv. Funct. Mater.* **2004**, *14*, 865–870.
- (67) Shaw, P. E.; Ruseckas, A.; Samuel, I. D. Exciton Diffusion Measurements in Poly (3-Hexylthiophene). *Adv. Mater.* **2008**, *20*, 3516–3520.
- (68) Spinelli, P.; Hebbink, M.; De Waele, R.; Black, L.; Lenzmann, F.; Polman, A. Optical Impedance Matching Using Coupled Plasmonic Nanoparticle Arrays. *Nano Lett.* **2011**, *11*, 1760–1765.
- (69) Krishnamoorthy, S.; Krishnan, S.; Thoniyot, P.; Low, H. Y. Inherently Reproducible Fabrication of Plasmonic Nanoparticle Arrays for SERS by Combining Nanoimprint and Copolymer Lithography. *ACS Appl. Mater. Interfaces* **2011**, *3*, 1033–1040.
- (70) Davies, P. M.; Hamm, J. M.; Sonnefraud, Y.; Maier, S. A.; Hess, O. Plasmonic Nanogap Tilings: Light-Concentrating Surfaces for Low-Loss Photonic Integration. *ACS Nano* **2013**, *7*, 7093–7100.